



Transport properties of 3D printed cementitious materials with prolonged time gap between successive layers

J. Van Der Putten^{a,*}, M. De Volder^a, P. Van den Heede^a, M. Deprez^b, V. Cnudde^{b,c},
G. De Schutter^a, K. Van Tittelboom^a

^a Magnel-Vandepitte laboratory for Structural Engineering and Building Materials, Department of Structural Engineering and Building Materials, Faculty of Engineering and Architecture, Ghent University, Technologiepark Zwijnaarde 60, B-9052 Ghent, Belgium

^b PProGress – UGCT, Department of Geology, Faculty of Science, Ghent University, Krijgslaan 281, S8, B-9000, Ghent, Belgium

^c Chairholder “Porous media imaging techniques”, Department of Earth Sciences, Faculty of Geosciences, Utrecht University, Princetonlaan 8A, 3584CD Utrecht, the Netherlands

ARTICLE INFO

Keywords:

3D printing
Durability
Carbonation
Chloride ingress
Freeze-thaw resistance

ABSTRACT

3D concrete printing is a promising additive manufacturing technique, integrated in construction industry to improve the geometrical complexity without expensive formworks. Due to the layered extrusion of the material, the porosity increases. This makes the component more prone to shrinkage and crack formation and increases the preferential ingress paths for aggressive substances. This can affect the durability and microstructure of the printed elements in a negative way. To assess the durability of 3D printed materials, three deterioration mechanisms (i.e. chloride ingress, carbonation and freeze/thaw) are investigated, considering different time gaps (i.e. 0 and 30 min) in between the layers and a comparison with traditional cast specimens was made. It was found that the resistance of 3D printed specimens against the penetration of chemical substances decreases with an increasing time gap. Compared with cast specimens, a higher saturated mass after frost attack could be observed in case of printed specimens.

1. Introduction

3D concrete printing (3DCP) is one of the advanced additive manufacturing (AM) technologies which tends to reform the construction industry into a modern and digitized industry with unprecedented design and geometrical freedom. Currently, the most widely adopted additive manufacturing technique for 3DCP is extrusion-based printing, where cementitious filaments are deposited onto one another until the desired object is realized [1]. Although this technology seems very promising for the construction industry, there are two principal reasons for concern. First of all, due to the lack of formwork, printed elements are directly exposed to environmental conditions (wind, rain, variable temperatures, carbon dioxide, etc.) which will reinforce the occurrence of (plastic) drying shrinkage, resulting in a higher degree of undesired deformations. In addition, the deformation of a new layer is (partly) hindered by the previous one. As a consequence, shrinkage stresses and cracking as well as their mitigation become increasingly important as they create preferential ingress paths for harmful substances. Secondly, due to the printing process, more pores and air voids are introduced,

both within the filament (intra) as in between the layers (inter) and this effect is more pronounced in case of higher time gaps [1–3]. Compared to conventionally cast concrete elements, the pores in printed structures are spatially not homogeneously distributed and may vary in pore size and pore size distribution. Additionally, as already stated by the authors [2], a changing pore morphology can be observed at the interface as there are more elongated pores/air voids parallel to the length of the filament. The effect of the latter on the mechanical performance has already been investigated thoroughly [4–8]. However, in terms of durability, a lot of parameters are still unknown.

Chloride ingress, carbonation and the resistance against freeze/thaw attack are three deterioration mechanisms frequently used to evaluate the long-term behavior of a structural component. First of all, chloride ions are one of the most harmful substances as they can initiate and propagate corrosion of the reinforcement. The integration of reinforcement in printed elements is at this moment still under development. However, as many researchers aim a full incorporation of this manufacturing technique in construction industry, this deterioration mechanism will become increasingly important in the near future. In

* Corresponding author.

E-mail address: Jolien.vanderputten@ugent.be (J. Van Der Putten).

<https://doi.org/10.1016/j.cemconres.2022.106777>

Received 31 May 2021; Received in revised form 10 March 2022; Accepted 11 March 2022

Available online 17 March 2022

0008-8846/© 2022 Elsevier Ltd. All rights reserved.

general, there are two main causes for the presence of chlorides in concrete: either they are incorporated in the composition during mix preparations (i.e. in the mixing water), which can be easily avoided nowadays, or they are transported into the material from the environment (i.e. by seawater and/or deicing salts). Like traditional concrete, the permeation properties which play a crucial role in assessing its durability characteristics, can be governed by various transport mechanisms such as capillary suction (absorption), concentration differentials (diffusion) and a difference in pressure between the inside of the concrete and its external environment. The dominating transport mechanism is dependent on the boundary condition, such as moisture content [9]. For conventional concrete, the transport of harmful substances occurs initially through absorption. In case of printed specimens, however, the interconnected pores at the interface and the microcracks in the printed surface may lead to an additional capillary suction. The movement of the water front will be affected by various parameters such as initial moisture condition at the interface, interlayer time gap, printing speed, etc. This phenomenon is also confirmed by Bran Anleu [10], who visualized the chloride penetration in printed specimen based on μ -XRF mapping and observed a pronounced ingress at the interlayers. The curing conditions of the specimens were also found to strongly influence the chloride penetration depth. After this first penetration stage, water migrates inwards the bulk material and the ionic transport at this stage can be primarily diffusion controlled. However, unlike conventional concrete, the effective surface area will increase for printed specimens as not only the exposed surface but also the saturated top and bottom of the interlayer will contribute in the process. This increased effective surface may have a positive effect on the diffusion rate in the bulk concrete. Due to the heterogenous distribution of the pores in printed elements, the transport mechanism will become even more complex. More in depth investigations are required to state these assumptions.

Carbonation on the other hand is not investigated yet for 3D printed structures, however, the underlying physics remain the same. Carbonation occurs when CO_2 from the air diffuses into the concrete through the pore network and reacts with alkaline constituents present in the concrete matrix such as calcium hydroxide (CH). This reaction produces calcium carbonate (CaCO_3) and leads to a pH reduction from 13 to around 9. The formed CaCO_3 , will further precipitate into the pores and will lead to a decrease in porosity as the volume of the formed calcite is approximately 12% greater than the volume of the original CH [11]. However, as stated by many researchers [12–14], there is an evidence that CO_2 reacts simultaneously with CH and calcium silicate hydrate (CSH). The microstructural changes in case of CSH carbonation are believed to differ highly from the porosity reducing effect of CH carbonation, as the polymerization of silicate chains in CSH may cause a volumetric decrease (shrinkage) as well as cracking and a coarsening of the pore structure. Depending on the binder system, one of the above-mentioned phenomena will become more dominant. For example, in case of pure Portland Cement (PC), there is a general agreement that CH carbonation is prevailing and the resulting formation of more voluminous calcite easily compensates for any decalcification shrinkage phenomenon inherent to CSH carbonation. Combinations of cement and mineral additions on the other hand, which are common in printed structures, are characterized by a higher porosity after carbonation. The CO_2 absorption will be affected by the layered print process as this will create, similar as for chloride intrusion, a higher exposure surface area. In addition, as stated by the authors in previous research [2], a prolonged time gap might also change the hydration products at the interface, which might also affect the CO_2 intrusion. However, this statement is to be confirmed.

Similar as for the above-mentioned deterioration mechanisms, the entire pore structure plays a crucial role when considering the frost resistance of a tested specimen; water freezing in the capillary pores defines the developed pressure, yet, the presence of air voids is able to mitigate those harmful stresses. When the resulting stresses in the

cementitious material would become too high, it can induce internal cracking [11,15]. However, this depends primarily on the transport rate of water (vapor) between the pores and the climatic boundary conditions, such as minimal temperature, cooling rate, water content, duration of freezing, etc. Out of the limited literature dealing with freeze/thaw resistance in 3DCP, it was revealed that compressive strength, depth of initial penetration, absorption capacity, absorption rate and the size of air voids are the deciding factors in the freeze thaw resistance [16,17]. In addition, the interface between successive layers came out as the most vulnerable to frost attack and risks of delamination. More specifically, the rate of bond drop was found 2 to 3 times higher than the drop in compressive strength [18].

Even after a thorough perusal of the existing literature, almost no laboratory or field studies could be found on transport-related deterioration issues. This highlights the need for such studies to gain further insights about the transport mechanisms and service life predictions for 3D printed structures. Within the scope of this research, the effect of the printing process on the transport mechanisms was investigated by varying the time gap (0 and 30 min) and a comparison with traditional cast cementitious materials was made. The chloride diffusion and CO_2 diffusion test were performed on four-layered specimens and the ingress was visualized on split samples by means of colorimetric measurements, while a quantification of the total chloride content was obtained by potentiometric chloride titrations. The freeze/thaw resistance of the specimens was evaluated based on mass loss and change in structural behavior.

2. Methodology

2.1. Mortar composition and printing process

A combination of Portland cement (CEM I 52.5 N, $\rho = 3160 \text{ kg/m}^3$), standard siliceous sand (CEN-Standard Sand according to EN 196-1, $D_{\text{max}} = 2 \text{ mm}$), water ($W/C = 0.36$) and a polycarboxylate superplasticizer (SP) (Glenium 51, con. 35%, BASF, Germany) was used. The mix composition is represented in Table 1.

To ensure proper dispersion of the dry materials, cement and sand were mixed in advance for 30 s at 140 rotations per minute (rpm) by using a planetary mortar mixer (Macben). Secondly, a predefined amount of water and SP were added and mixed for 30 s at the same mixing speed, followed by a more intensive mixing period (285 rpm) during 30 s. After scraping the edges of the bowl for 30 s, the material was allowed to rest for 1 min. The mixing procedure ended with an intensive mixing period for 60 s at 285 rpm.

After mixing, the cementitious material was inserted into a Quick-point mortar gun, used to simulate an extrusion-based 3D printing process. The mortar gun was composed of a container to insert the mixture, a Black&Decker 5.2 Amp drill build-in and an auger to move the cementitious material towards the cylindrical nozzle ($18 \times 28 \text{ mm}^2$). The mortar gun was vertically mounted on a movable building platform and could be altered in height to provide the required distance between the nozzle and the building platform. The rotational speed of the auger could be regulated manually and was chosen in accordance with the applied printing speed, the translational motion of the building platform was controlled by a complementary software program. Within the scope of this research, the printing speed equals 3.0 cm/s. The layer height and length were fixed at 10 mm and 300 mm, respectively. In order to fulfill the extrudability requirements [2], deformations not exceeding 10% of the nozzle dimensions were accepted during printing.

Sample preparation started by the extrusion of a substrate layer ($l =$

Table 1
Composition of 3D printable cementitious material [kg/m^3].

Component	CEM I 52.5	Sand 0/2	Water	SP
Amount [kg/m^3]	625	1241	227	1.2

300 mm) on a standard glass base plate without pretreatment. After changing the vertical position (Z-position) and after waiting for the defined interlayer time interval (i.e. 0 or 30 min), the second layer was extruded on top of the previous one. The latter was deposited at the same horizontal position to ensure a similar time gap in between every position of the printed layer. Specimens with a zero minutes time interval were fabricated with the same batch of material, while in case of a 30-minutes time gap a new batch of material was applied to ensure similar rheological properties. Printed samples were stored in climatized conditions (20 ± 2 °C and $65 \pm 5\%$ RH) until the day of testing. To compare the behavior of printed samples with traditional cast mortars, prismatic molds ($160 \times 40 \times 40$ mm³) were filled in two steps and compacted by jolting 60 times. The molds were covered with foil during 24 h and demolded after 24 h. Thereafter, the prisms were stored under the same conditions as mentioned before (20 ± 2 °C and $65 \pm 5\%$ RH) until the day of testing.

2.2. Microstructural analysis

Pore characterization (size and distribution) is a key aspect for durability investigations. Therefore, X-ray micro-computed tomography (μ CT) was performed at the Ghent University Centre for Tomography (UGCT) using HECTOR [19], which comprises a micro focus directional target X-ray source (X-ray WorX XWT 240-SE), a large flat-panel detector (40×40 cm²; PerkinElmer 1620 CN3 CS). An aluminum filter of 1 mm which was placed in front of the X-ray source to reduce beam hardening artefacts. Cylindrical sample ($\varnothing = 14$ mm; $h = 20$ mm) were drilled out of an original two layered printed sample. During image acquisition, HECTOR operated with a tube voltage of 200 keV and a tube power of 10 W. The resulting magnification and the voxel size equaled 24.64 and 8 μ m, respectively, and 2401 projections were taken per scan. The cast sample was shaped differently (i.e. squared instead of cylindrical), and therefore, an alternation of the applied scan parameters was required. For this sample, the power was increased until 11 W, the amount of projections until 2601 per scan and the magnification and voxel size until 17.92 and 11 μ m. To image the total sample volume with the highest possible spatial resolution, the top and bottom half of each sample were imaged separately. Reconstruction of the raw CT data was done using Octopus Reconstruction software [20]. Afterwards, Aquila software (Tescan XRE) was used to merge the sets of two reconstructed volumes per sample into one. Image analysis to determine the porosity and pore sizes was done using Avizo software (ThermoFisher Scientific).

2.3. Chloride diffusion test

Chloride diffusion tests were performed in accordance with CEN/TS 12390-11 [21], both on cast specimens and four-layered printed samples. The first and fourth layer of the latter were mainly used to avoid side effects, as mainly the ingress of aggressive substances through the interlayer is the scope of interest. After a hardening period of 21 days, samples were dry-cut into specimens with a total length of 40 mm. Dry-sawing was preferred to avoid any disruptions due to moisture condition. To ensure unidirectional diffusion, 5 of the 6 sample sides were coated with an epoxy resin (Episol Designtop SF, Resiplast NV), carried out in two layers with a waiting time of 24 h in between (Fig. 1).

At the age of 28 days, samples were immersed in a 3% by mass aqueous sodium chloride (NaCl) solution for a maximum of 70 days. Evaporation of the solution was prevented by storing the samples in sealed boxes and the solution was changed on a monthly base. The uncoated sample side was placed upwards in the solution. Contradictory to CEN/TS 12390-11, samples were not saturated with $\text{Ca}(\text{OH})_2$, this in order to simulate more realistic exposure conditions. Furthermore, as a faster chloride penetration is expected in case of printed elements due to the higher porosity, samples were taken out of the solution on a weekly base, starting at one week till ten weeks after exposure. The latter is in contrast with the standard procedure as prescribed by [21]. The ingress of chloride ions was examined in two ways. The chloride penetration front was visualized based on a colorimetric method and a quantification of the chloride content was obtained by performing potentiometric chloride titrations.

2.3.1. Colorimetric method

On a weekly base, three samples of every test series were split perpendicular to their print direction. On the freshly broken specimens, an aqueous silver nitrate solution (AgNO_3 , conc. 0.1 mol/l) was sprayed. Afterwards, two well-defined regions could be easily distinguished. The first region, discolored to white, visualizes the penetration depth of the free chlorides and is referred to as the chloride-affected zone. The second region appeared to turn brown by a brown silver oxide precipitate, generated by immediate decomposition of silver hydroxide [9] and corresponds with the region assumed to be free of chlorides. However, this second region is not completely chloride-free as the discoloration only happens at a certain chloride concentration which equals, as stated by Real et al. [22], 0.01% up to 1.14% by mass of cement. Note that this concentration depends on many factors, such as type of cement, water-to-binder ratio, concrete age, spray amount and AgNO_3 solution

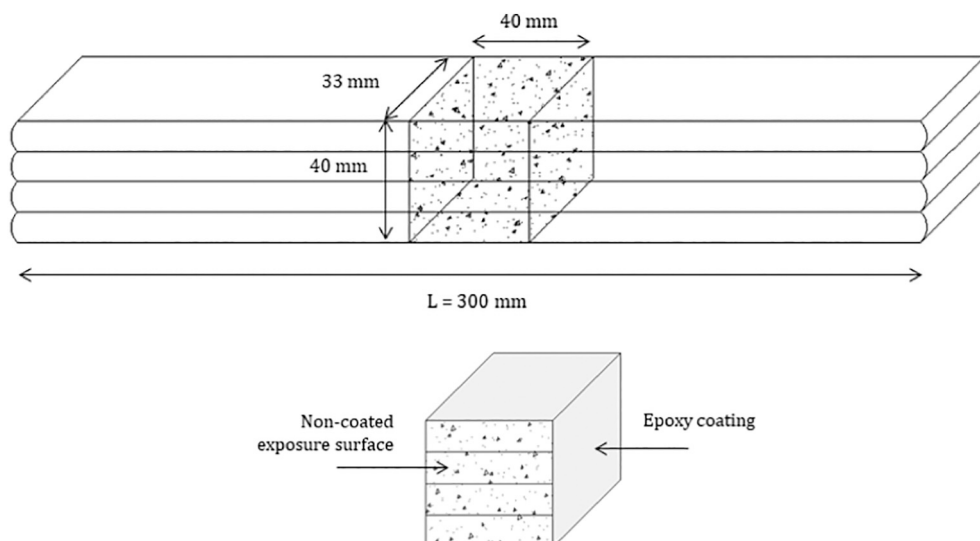


Fig. 1. Schematic representation of a printed sample, saw-cut from a four-layered printed specimen, indicating the coated and non-coated surfaces.

concentration.

The chloride penetration was evaluated based on the penetrated area and depth. The latter parameters were determined by applying a custom-made plugin in ImageJ, after imaging both halves of the split surfaces. The quantification of the penetrated area is visualized in Fig. 2A. A similar procedure was followed for cast and printed specimens. The chloride penetration depth in case of a printed sample was measured at the second and third layer only in order to exclude side effects. Therefore, every millimeter, three points were placed on the photograph, indicating the outer boundaries of the sample and the boundary between chloride-affected and chloride-free zone (Fig. 2B). As one assumes a homogenous material in case of cast samples, the chloride penetration depth was measured over the entire sample height and the measuring points were placed at a 2 mm interval (Fig. 2C).

2.3.2. Chloride titrations

A quantification of the chloride content was obtained based on potentiometric titrations. At the second interlayer, nine layers parallel to the exposed surface were ground off with a diamond coated drill head (8 mm in diameter) and the layer depth of the first and following layers equaled 5 and 3 mm, respectively. Before titrations, the powders were dried in an oven at 105 °C for at least 7 days (Fig. 3).

The total chloride content of each layer was determined by acid-soluble extraction in a nitric acid (HNO₃) solution, followed by a potentiometric titration [9,11]. The latter was performed by using a Metrohm 862 Compact Titrosampler automatic titrator with 0.01 mol/l silver nitrate as titration solution. The automatic titration device adds AgNO₃ to the test solution until the point of equivalence of the reaction (Ag⁺ + Cl⁻ → AgCl↓). This point is characterized by a sudden change in the potential of the solution, measured by means of a combined silver ring electrode. Before the automatic titration could be executed, the exact concentration of the AgNO₃ solution was determined based on a calibration. The measured AgNO₃ volume was implemented in Eq. (1) to calculate the exact concentration, assuming that the concentration and volume of the standard NaCl calibration solution equal 0.01 mol/l and 0.005 l, respectively.

$$\text{Conc AgNO}_3 \text{ (mol/l)} = \text{Conc NaCl (mol/l)} \cdot \frac{\text{Vol NaCl (l)}}{\text{Vol AgNO}_3 \text{ (l)}} \quad (1)$$

Based on this calibration, the resulting acid-soluble chloride content of each layer was calculated according to Eq. (2).

$$c_t = \frac{35.45 \cdot V_{\text{AgNO}_3} \cdot c_{\text{AgNO}_3}}{m_{\text{powder}}} \quad (2)$$

within this equation:

- c _t	Acid-soluble chloride content	[m% binder]
- 35.45	Atomic mass of chloride	[g/mol]
- V _{AgNO₃}	Consumed volume of the AgNO ₃ solution	[ml]
- c _{AgNO₃}	Exact concentration of AgNO ₃ after calibration	[mol/l]
- m _{powder}	Mass of concrete powder in the extraction solution	[g]

A complete titration profile was obtained by plotting the measured acid-soluble chloride content against the depth below the exposure surface. The non-steady state diffusion coefficient D_{NSS} [m²/s] and the surface concentration c_s [m% binder] were estimated by fitting Eq. (3) to the measured chloride contents by using non-linear regression analysis. The latter was performed according to the method of least squares fit using SPSS Statistics 27 software. In order to have an appropriate fit and to take into account the fast chloride ingress due to the use of non-saturated samples, the first points of the profile (i.e. 0–5 mm and 5–8 mm) were omitted from the overall shape of the profile.

$$C(x, t) = C_s - (C_s - C_0) \cdot \text{erf}\left(\frac{x}{2 \cdot \sqrt{D_{\text{NSS}} \cdot t}}\right) \quad (3)$$

with:

- C(x, t)	Chloride concentration at depth x and time t	[m% binder]
- C _s	Chloride concentration at the exposed surface	[m% binder]
- C ₀	Initial chloride concentration	[m% binder]
- erf(.)	Error function	[-]
- x	Distance from the exposure surface until the center of the layer	[m]
- t	Time the sample is exposed to 3% NaCl solution	[s]
- D _{NSS}	Non-steady state diffusion coefficient	[m ² /s]

The latter equation was simplified by replacing the error function by an approximate cumulative normal distribution (Eq. (4)).

$$C(x, t) = C_s - 2(C_s - C_0) \cdot \left[\Phi\left(\frac{x}{2 \cdot \sqrt{D_{\text{NSS}} \cdot t}}\right) - \frac{1}{2} \right] \quad (4)$$

2.4. Carbonation test

Carbonation tests were performed in accordance with CEN/TS 12390-10 [23], both on four-layered printed specimens and cast samples. After a hardening period of 7 days, specimens were saw-cut (l = 40

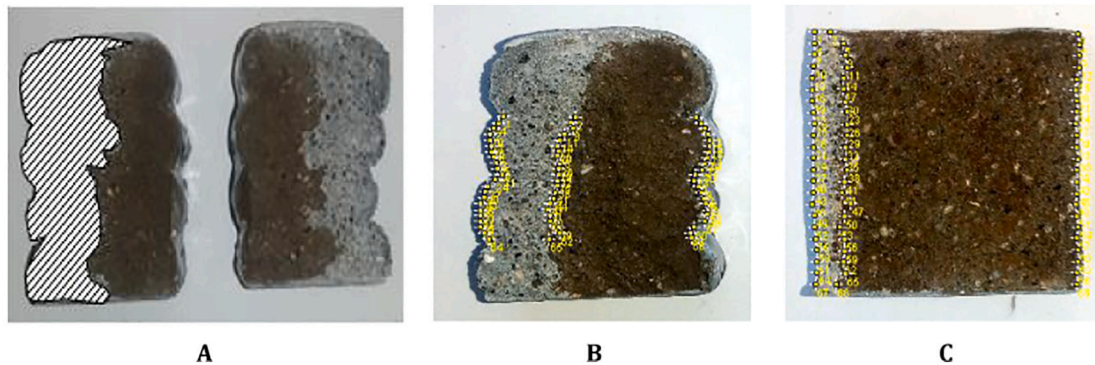


Fig. 2. Chloride penetration area (A) and a representation of the measuring points used for ImageJ analysis in case of printed elements (B) and molded specimens (C).

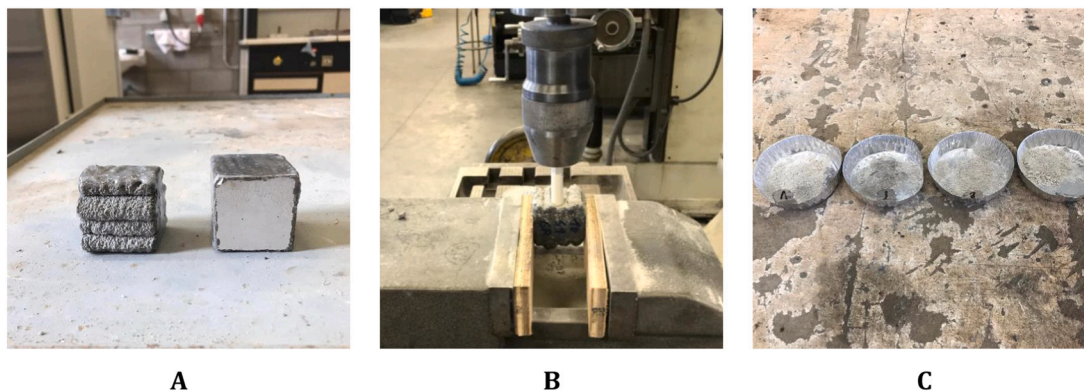


Fig. 3. Representation of the grinding process with (A) the coated specimens, (B) the 8 mm drill and (C) the powders used for potentiometric titrations.

mm) and coated with epoxy (Episol Designtop SF, Resiplast NV), which was carried out in two layers on 5 of the 6 sample sides with a waiting time of 24 h in between (Fig. 1). The coated elements were placed in a carbonation chamber (20 ± 2 °C and $60 \pm 5\%$ RH) containing 1 vol% CO_2 at the age of 12 days. After one, three and twelve weeks of exposure, three samples of every test series were split perpendicular to their print direction and a 1% phenolphthalein solution was deposited on the freshly broken surfaces. The carbonated area stayed colorless, while the non-carbonated region turned purple. The transition point for the phenolphthalein is situated when the pH-value ranges in between 8 and 9.8, which implies that there is still a risk of underestimating the actual carbonation depth. A quantification of the penetration depth is determined based on ImageJ analysis, with the same plugin as used for chloride intrusion.

2.5. Freeze/thaw resistance

The resistance against freeze/thaw was evaluated according to NBN B 15 – 231 [24]. After 28 days, the two-layered specimens and traditionally cast prisms were sawn into specimens with a total length of 40 mm and submerged in water until complete capillary saturation (i.e. mass difference lower than 0.1% after 24 h). Thereafter, half of the samples were placed in a low-temperature chamber for 14 successive freeze/thaw cycles. The temperature reached a minimum and maximum of -5 °C and 20 °C, respectively within every cycle of 24 h. After this series of cycles, samples were saturated again until 100%, as described supra. The resistance against freeze/thaw was evaluated based on changes in mass and compressive strength before and after 14 freeze/thaw cycles.

The compressive strength f_c [N/mm^2] was measured on cylindrical specimens ($\varnothing = 25$ mm; $h = 20$ mm), drilled from prismatic specimens, and was investigated perpendicular to the print direction. The test was executed in a Walter+Bai DB 250/15 hydraulic testing machine (NBN EN 12390-3 [25]), under load control with an incremental rate of 100 N/s. Before testing, both top and bottom surface were mechanically flattened to ensure parallelism (accuracy of 0.05 mm). In addition, 3 mm thick high-density fiberboard plates were put in between the bases and the hydraulic system. The compressive strength was tested in triplicate for every series and the loss in compressive strength was calculated based on Eq. (5), where D (%) is the loss percentage of the compressive strength, $f_{c,0}$ [N/mm^2] is the average strength for samples without freeze/thaw deterioration and $f_{c,14}$ [N/mm^2] is the compressive strength measured after 14 cycles.

$$D (\%) = \left[\frac{(f_{c,0} - f_{c,14})}{f_{c,0}} \right] \quad (5)$$

2.6. Statistical analysis

Based on SPSS statistics 26, the obtained results were statistically analyzed. The means were compared by performing an independent samples t -test. When comparing multiple means, an Analysis of Variance (ANOVA) was executed. The homogeneity of the variances was studied on the basis of a Levene's test. In case of homogeneous variances, the multiple comparison test of Student-Newman-Keuls was performed. When the variances were not homogeneous, a Dunnett's T3 test was performed. Based on this analysis, one could conclude whether the results were significantly different or not. The level of significance equaled each time 5%, unless specified otherwise.

3. Results and discussion

3.1. Microstructure

Fig. 4 represents profiles of the volume fraction of air voids for each XY plane of the μCT data over the height of the sample (Z). From these profiles, two general conclusions can be made. First, by comparing REF with T0, a lower air void volume fraction can be observed in case of traditional cast specimens (approximately 1.68% compared with 5.65%) due to the applied compaction during manufacturing of the samples. The air voids are in both cases more or less homogeneously distributed through the specimen, minimizing the anisotropic behavior of the material when printing two layers directly upon each other. The amount of air voids in the bulk material is comparable, independent of the applied time gap. Unlike specimens with a zero-minute time gap, a significant increase in air voids can be observed at the interlayer for longer waiting times. Furthermore, μCT imaging is also useful to visualize pores in 3D (Fig. 6). Here, all voids with a diameter larger than 100 μm and a flatness between 0.1 and 0.45 are displayed (0 is totally flat, 1 is round) and based on this, a change in pore morphology can be observed and quantified. The interlayer contains more flat and elongated pores due to the moisture exchange and the lack of structural stability. The occurrence of flat pores in the molded specimens is negligible.

3.2. Chloride diffusion test

3.2.1. Colorimetric measurements

A first visualization allows the classification of the profiles based on the location and depth of the chloride ingress. Class A represents a homogeneous, equidistant penetration front from the exposure surface onwards over the entire height of the sample (Fig. 6A). Samples of class B show a more local penetration at the interlayer, while characteristic samples for class C show chloride penetration up to the opposite coated side through the interlayer (Fig. 6B and Fig. 6C). Class D represents a full penetration through the entire bulk material (Fig. 6D). Table 2 represents the percentages of the different samples, both cast and printed,

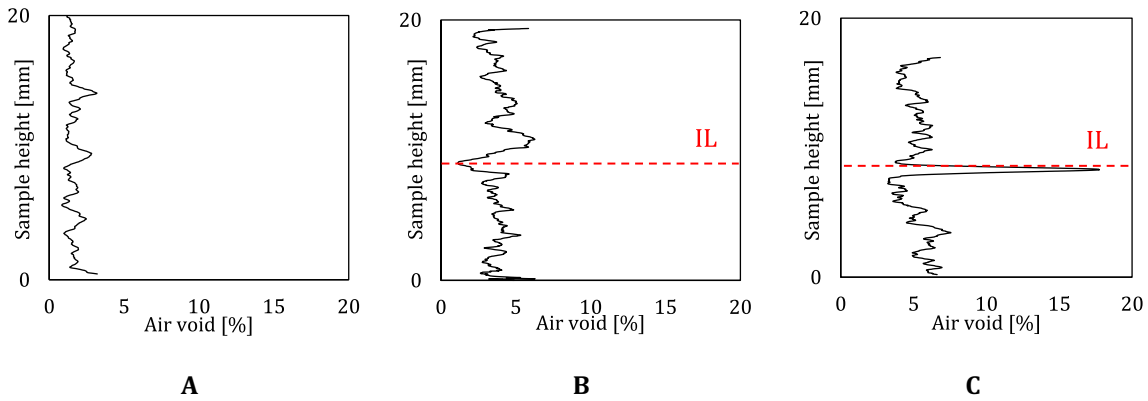


Fig. 4. Air void volume (%) in case of a traditional cast specimen (A), specimens printed with a 0 min (B) and 30 min (C) time gap, measured by μ CT-scanning at the age of 28 days ($n = 1$). The position of the interlayer (IL) is indicated by a red line. (For interpretation of the references to colour in this figure legend, the reader is referred to the web version of this article.)

Table 2

Classification of the different samples (% , $n = 6$), produced by traditional casting (CAST) or by printing with different interlayer time gaps (T0 and T30).

	A	B	C	D
CAST	100%	/	/	/
T0	87%	13%	/	/
T30	27%	60%	10%	3%

belonging to the different classes.

An equidistant penetration front can be observed in case of traditional cast concrete and samples printed with a zero-minute time gap, indicating that for both manufacturing techniques a homogeneous material is obtained. This is also stated by the results represented in Fig. 5,

where a continuous distribution of the air voids can be observed. On the other hand, as the time gap increases, the penetration at the interface becomes more pronounced and in case of 30-minutes time intervals, chloride penetration through the interlayer up to the opposite coated site is possible. This phenomenon can be attributed to the higher amount of pores at the level of the interlayer.

Fig. 7 represents the area penetrated by chlorides, starting from one week until ten weeks after exposure. One can see that cast samples are less prone to chloride penetration. After one week of chloride intrusion, only 15% of the area is penetrated, compared with 31% and 54% in case of T0 and T30, respectively. The fast intrusion in case of printed samples can be attributed to the increased surface area exposed to capillary absorption (i.e. exposure surface and interlayer), as mentioned in the introduction. Additionally, 3D printed elements are directly exposed to

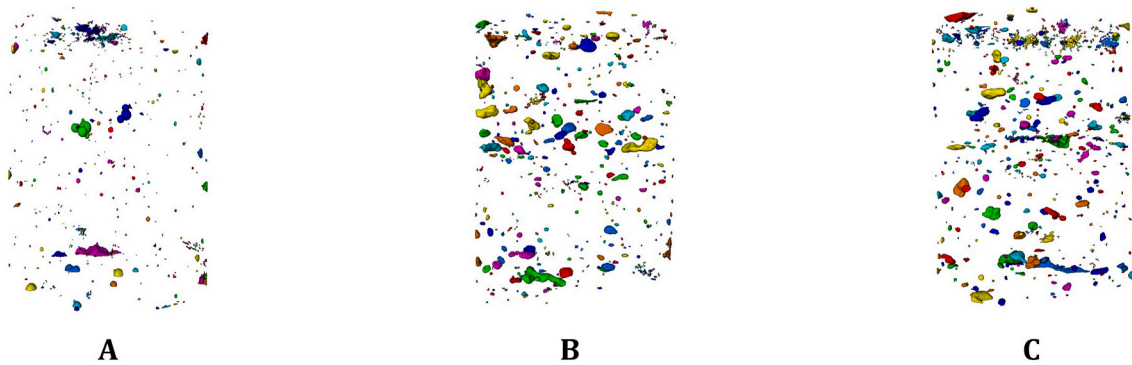


Fig. 5. 3D rendering of air voids with a flatness between 0.1 and 0.45 obtained with Octopus reconstruction software in case of molded specimens (A) and specimens printed with a 0 (B) and 30 min (C) time gap ($n = 1$).

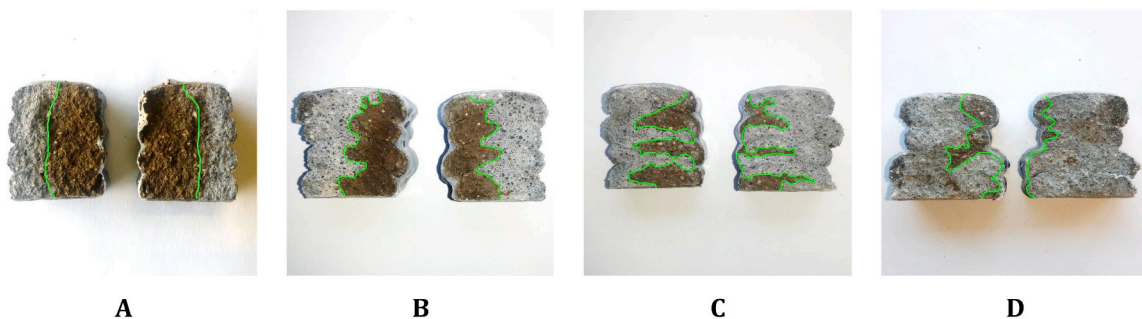


Fig. 6. Classification of the chloride penetration profiles in four classes: (A) equidistant penetration from the exposure surface, (B) local penetration at the interlayer, (C) chloride penetration up to the opposite coated side through the interlayer and (D) chloride penetration up to the opposite coated side through the bulk material.

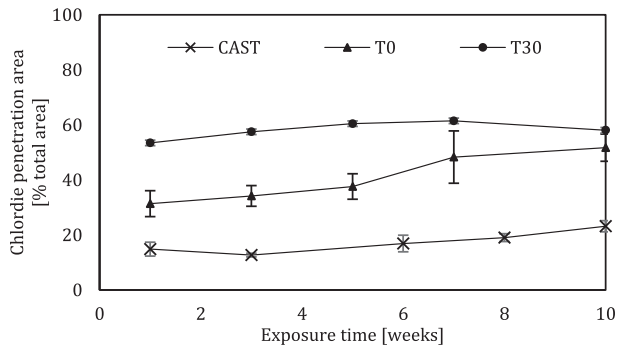


Fig. 7. Chloride penetration rate as a function of the exposure time for cast and printed specimens ($n = 6$, error bars represent standard deviation).

environmental conditions due to the lack of molding. The latter results in higher evaporation of the bleeding water, a lower moisture content [2,6] and a higher degree of (drying) shrinkage and related crack formation [26].

Samples printed with a prolonged time gap will end up with a higher surface tension acting on the capillaries due to a higher moisture exchange and a higher amount of microcracks at the surfaces. Although these microcracks are not directly measured in this paper, this assumption is confirmed by Moelich et al. [26], where a higher number of cracks with larger crack widths could be observed in the printed surface during the first 2.5 h after printing. These cracks cannot occur in case of mold-cast elements, as in general these specimens are demolded only after 24 h of hardening. Hence, more preferential ingress paths are introduced and the penetration of chloride ions will proceed much faster. Nevertheless, the rate of chloride ingress stagnates after a few weeks due to chloride binding. This relatively fast binding process, comparable to diffusion, initiates the formation of Friedel's salt which alters the pore structure and decreases the porosity [27]. The effect of the weak interface is also observed in Fig. 8, representing the exact penetration depth measured from the exposure surface over the second and third layer.

3.2.2. Potentiometric titrations

Potentiometric titrations were performed every two weeks and the chloride penetration profile was obtained by plotting the measured chloride concentration versus the depth below the exposed surface. Subsequently, a mathematical profile, based on the solution to Fick's second law of diffusion is fitted to the measured profiles. Before going

deeper into the results, a couple of remarks should be made. First, for optimal comparison between the colorimetric measurements and the potentiometric titrations, measurements are preferably carried out on the same sample. Since this was practically not possible, the measurements were carried out on samples of the same batch, taken into account the large differences between the samples initiated by the printing process. Secondly, a direct comparison between both techniques is not possible, as colorimetric measurements visualize free chlorides, whereas in case of titration the acid-soluble chloride content is obtained. The latter value is more representative for the total chloride content.

Based on the results represented in Fig. 9, it can be concluded that the chloride content will stagnate to an almost constant value after a certain depth (approximately 15 mm). Regardless of the fabrication process, the total chloride content increases with an increased exposure time. As the samples were not saturated with $\text{Ca}(\text{OH})_2$, the chlorides enter the 3D printed specimens mainly through the porous interlayer and this causes a higher chloride content at larger depths below the exposed surface. Additionally, the total chloride content increases when extending the interlayer time interval. The complicated penetration mechanism (absorption + diffusion) leads to a portion chloride profile that cannot be modeled based on Fick's second law of diffusion, resulting in the formation of a local peak, located at the interior rather than at its surface. This phenomenon is referred to as the maximum phenomenon and it divides the concrete surfaces into two different layers with different predominant ionic transport mechanisms: the "skin" layer, where the chloride content increases with the sample depth and the internal or bulk material where the chloride profile fits into the Fickian behavior [28]. The skin effect can be attributed to the different composition of the outer surface of the printed elements, as already observed by the researchers themselves [2].

Based on the chloride profiles, it is not possible to determine the width of the skin layer and more in-depth investigations of the first 5 mm are required. However, this will be a difficult task due to the heterogeneity of the surface of the interlayer. Furthermore, carbonation of the exposure surface can occur during hardening and sample preparation. In such case, the carbonated phases in the skin layer have less binding capacity [29], leading to an apparent maximum in total chloride content just at the boundary of the skin layer and the bulk material. In addition to carbonation, also the physical adsorption of calcium (Ca^+) and chloride (Cl^-) on the silanol sites (SiOH) from CSH takes place. This behavior is enhanced for hydrated PC cement paste with a pH above 11.65. close to the surface, where the element is in contact with the chloride solution, there is a less favorable condition for chloride absorption due to the lower pH value. At deeper depths, the pH reaches higher values, enhancing the adsorption of calcium and chlorides which leads to the maximum chloride content peak. In order to improve the accuracy of the observations and conclusions, more in-depth investigations (e.g. fluorescence microscopy) are required.

Based on Eq. (3), the non-steady state diffusion coefficient D_{NSS} and chloride surface concentration C_s are obtained and summarized in Table 3. In general, it can be concluded that D_{NSS} decreases and the chloride surface concentration increases with increasing exposure time. These results are in accordance with literature. Based on the results, it can be observed that D_{NSS} is higher for printed samples and increases with increasing time gap.

However, the chloride concentrations at the surface exceed the concentration of the solution. The latter can be attributed to condensation phenomena induced by the existence of an electrical double layer (EDL) in the cement paste [11,30]. The EDL consists out of a diffuse layer, which is negatively charged and a compact layer which mainly consists of positively charged ions. Consequently, a difference in ionic concentration is established between the diffuse layer and the bulk solution. Furthermore, the chloride content in the diffuse layer is much higher than in the bulk solution which may explain why the chloride concentration at the surface exceeds the concentration of the exposure solution. Additionally, the large deviations observed in Table 3 can be

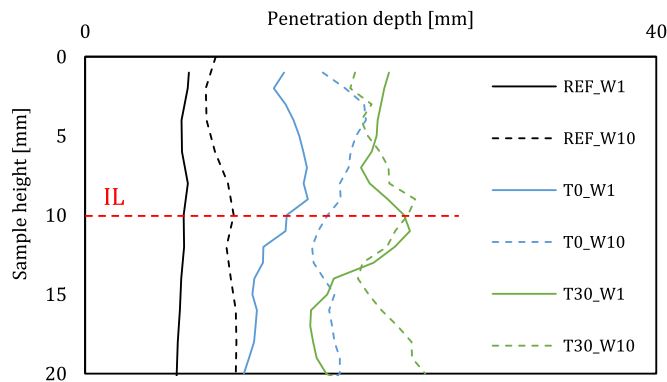


Fig. 8. Penetration depth [mm] as a function of the exposure time in case of traditional cast specimens and printed specimens ($n = 6$, error bars are left out for the sake of clarity), measured every 2 or 1 mm, respectively. The position of the interlayer (IL) is indicated by a red line. (For interpretation of the references to colour in this figure legend, the reader is referred to the web version of this article.)

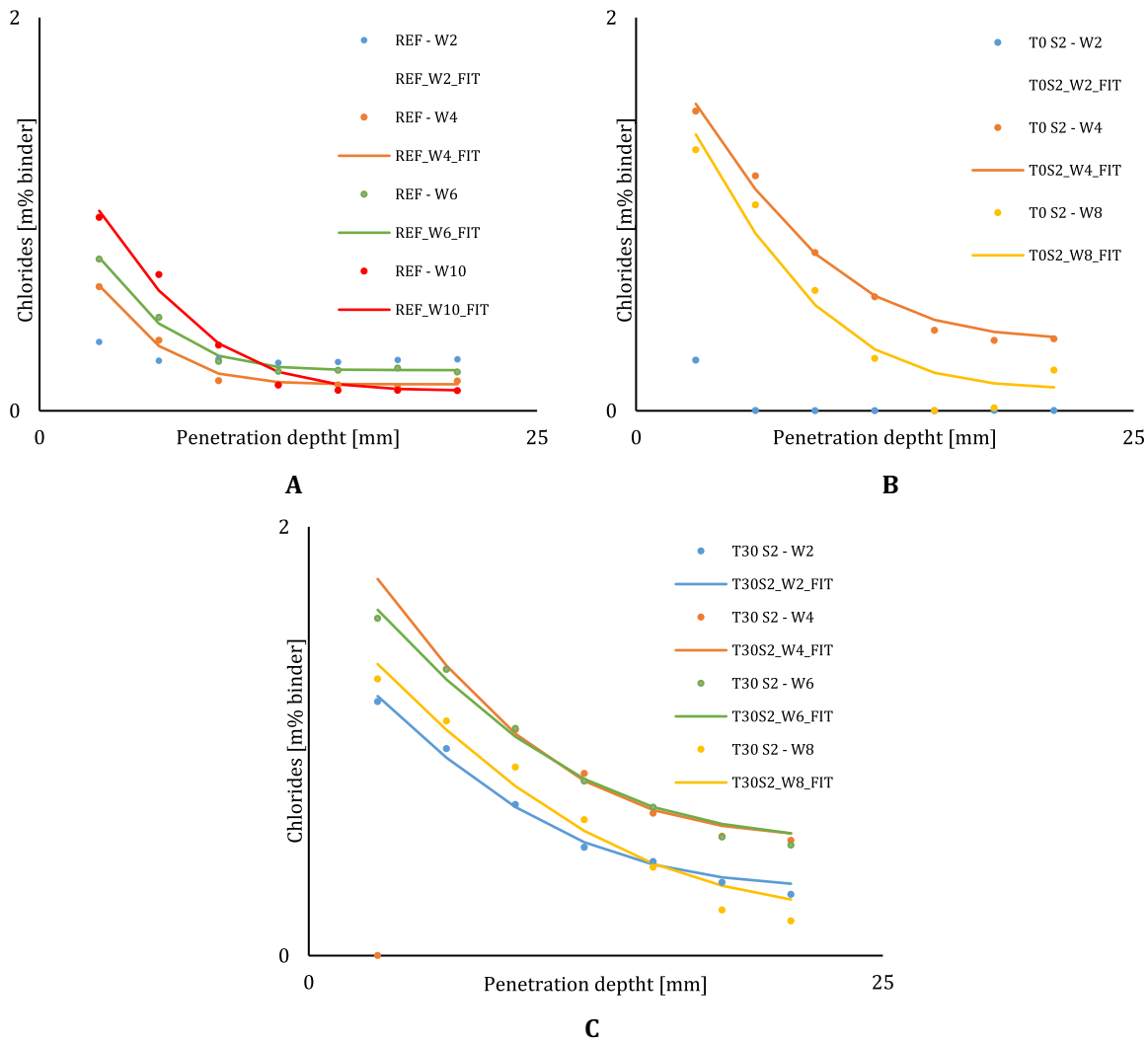


Fig. 9. Chloride penetration profiles in case of traditional cast specimens (A), specimens printed with zero-minute time gap (B) and 30 min time gap (C). Fittings of REF_W2 and T0S2_W2 were not included as there was only one point measured during titrations. Results of REF_W8, T0_W10 and T30_W10 were unreliable and left out.

Table 3

Evolution of D_{NSS} [$10^{-12} \text{ m}^2/\text{s}$] and C_s [m% binder] after different weeks of chloride exposure. Results of REF_W2 and T0S2_W2 were not included as there was no possible fitting. Results of REF_W8, T0_W10 and T30_W10 were unreliable and left out.

	D_{NSS} [$10^{-12} \text{ m}^2/\text{s}$]					C_s [m% binder]				
	W2	W4	W6	W8	W10	W2	W4	W6	W8	W10
REF	/	4.603	3.44	/	3.56	/	1.09	1.26	/	1.52
T0	0.49	13.05	7.63	5.81	/	/	2.06	6.36	5.41	/
T30	32.60	15.11	12.18	11.85	/	1.53	2.21	1.97	1.69	/

attributed to the irregularities of the individual samples.

3.3. Carbonation

Fig. 10 represents the carbonation depth as a function of time and a similar behavior can be observed as for samples exposed to chlorides. It is clear that specimens with a higher porosity will facilitate the penetration of CO_2 . Furthermore, due to CO_2 intrusion, the porosity of the samples will change. The smaller pores will be filled with calcium carbonate, which has a higher volume than the parent compounds of portlandite (CH) and calcium-silicate-hydrates (CSH), whereas larger pores appear between the calcium carbonate microcrystals, resulting in a

coarser microstructure after carbonation.

In case of cast specimens, the penetration depth is significantly smaller compared with the 3D printed samples. According to the statistical analysis, a vertical carbonation front (i.e. no significant difference in penetration depth along the height of the sample) is observed which confirms the assumption of a homogenous material. Nevertheless, notion should be taken that no carbonation front was visualized during the first three weeks of exposure. On the one hand, this observation can be attributed to the extensive compaction of the traditionally cast elements. On the other hand, the phenolphthalein indicator shows no discoloration when the pH value of the carbonated region does not drop below 9. As a consequence, cast specimens could already be partly

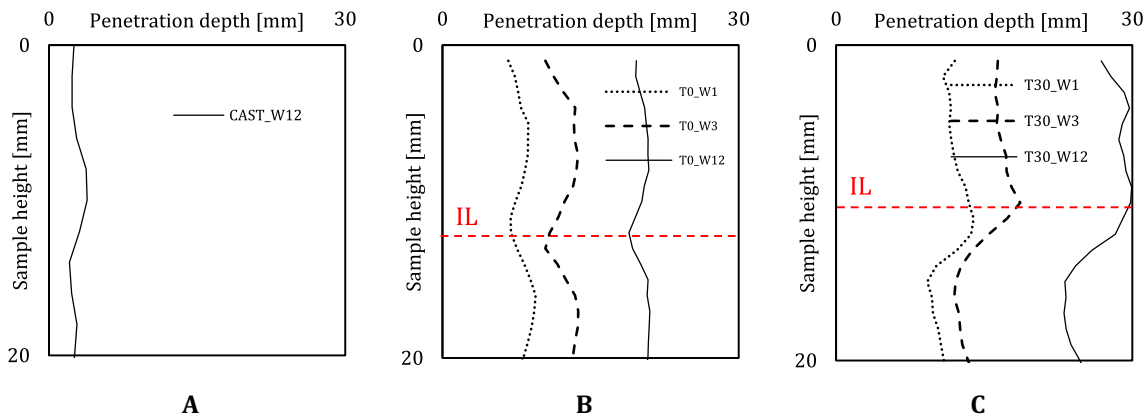


Fig. 10. Carbonation depth as a function of the exposure time in case of molded specimens (A) and specimens printed with a zero- (B) and 30-minute (C) time gap. The position of the interlayer (IL) is indicated by a red line. (For interpretation of the references to colour in this figure legend, the reader is referred to the web version of this article.)

carbonated during the first three weeks, whereas the pH did not cross the critical value.

Specimens printed with a zero-minute time gap show a deeper penetration of CO₂ but the ingress front can also be assumed as uniform as confirmed by statistical analysis. The latter can be attributed to the higher porosity of 3D printed samples and the formation of micro-cracks in plastic state of the material. A higher interlayer time interval increases the carbonation rate at the level of the interlayer as well as in the layers themselves. The higher porosity, the presence of micro-cracks and the interconnectivity of the pores leads to the higher carbonation depth as observed for the higher time gaps.

As resumed by Qui et al. [31], the above mentioned colorimetric test does not indicate the depth of maximum CO₂ and the actual carbonation depth could be underestimated. Furthermore, the accuracy of the ImageJ analysis could be improved as it depends on the quality of the picture and the interpretation of the researcher. To evaluate the magnitude of this underestimation, the penetration depth is preferably studied by for example thin sections and thermogravimetric analysis (TGA). However, these investigations require more preparation and are more labor intensive compared with the colorimetric measurements.

Based on the above-mentioned results, one can conclude that the resistance against chloride penetration and carbonation for 3D printed cementitious materials is generally inadequate. The durability performance can be increased by the application of a proper curing method, both external (e.g. application of a damp hessian or wetting the fresh material) or internal (e.g. the addition of superabsorbent polymers). It is also suggested in addition to control the shape of the layers more or to smoothen the outer surfaces to eliminate deviations related to the print geometry.

3.4. Freeze/thaw resistance

Table 4 represents the mass increase of the samples in full saturated state and the accompanied standard deviation between brackets. The mass increase is obtained at the age of 35 (m_{35} , $n = 18$) and 56 (m_{56} , $n = 9$) days after freeze/thaw attack. Molded specimens have a lower mass increase at the age of 35 days compared with printed samples, due to the

Table 4

Mass increase [%] after 14 freeze/thaw cycles ($n = 9$), measured in full saturated state.

	Δm_{35} [%]	$\Delta m_{56,freeze}$ [%]
CAST	1.33 (0.11)	1.58 (0.10)
T0	4.69 (0.18)	5.09 (0.12)
T30	4.01 (0.21)	4.29 (0.15)

lower porosity as stated before. As proven by statistical analysis, the mass increase of printed samples does not depend on the applied time gap.

During freezing, the interstitial solution does not freeze at a single temperature as a result of the nonhomogeneous pore size distribution, indicating that the material contains both nonfrozen water and ice. When a cementitious material is exposed to freezing temperatures, the pore water can start freezing, which results in the formation of ice and induces possible damage. Ice formation is initiated first in the larger pores within the capillary pore structure, expelling the pore water from the freezing pores due the volume increase of 9%, finding its way to air voids when the crystallization process starts. Due to the thermodynamic imbalances, the new ice crystals in the air voids start to grow and the water will attract water from the neighboring smaller pores and the transport is reversed. As the crystals have a lot of space to grow within the air void, there will be no or little crystallization pressure in this situation. Otherwise, the pressure can result in damage and cracking of the freezing concrete. Mercury intrusion porosity (MIP) measurements, performed by the authors in previous research [2], revealed that the critical pore size diameter (i.e. the steepest slope in the cumulative intrusion curve) is larger in case of specimens printed with a zero-minute time gap compared with 30-minutes time gaps. This observation can explain the higher water absorption when comparing the printed samples.

Based on a statistical analysis, the compressive strength seems not affected by the freeze/thaw cycles (Fig. 11). A first explanation of this phenomenon could be the increased amount of air voids at the interface and in the bulk material as a result of the print process. As a

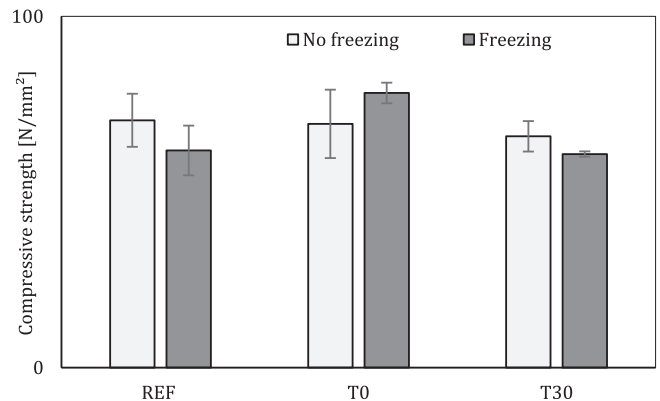


Fig. 11. Compressive strength [N/mm²] before and after freeze/thaw attack ($n = 3$, error bars indicate standard deviation).

consequence, more space is available to accommodate ice crystals without the crystals having to exert pressure on the pore walls. Therefore, the risk of damage seems smaller. Secondly, as observed in literature [18], the porosity of the samples is only minorly affected when the number of freeze/thaw cycles does not exceed 25 in total. The latter phenomenon highlights the fact that the number of freeze/thaw cycles, as prescribed in the current standards, has to be increased as the porosity in the first stage is already higher and damage will be induced in a later stage.

4. Conclusions

Within the scope of this research, the durability of molded specimens was compared with 3D printed cementitious materials based on the resistance against chloride ingress, CO₂ penetration and the resistance against freeze/thaw. Based on the results, the following conclusions can be made:

- The air void content of printed samples (> 75 μm) is higher compared with conventional concrete. For both molded specimens and specimens printed with a zero-minute time gap, a uniform distribution of the air voids could be observed. A prolonged time gap increased the porosity at the interface, creating weak interfaces;
- For both deterioration mechanisms (i.e. intrusion of chlorides and the penetration of CO₂), a similar penetration could be observed: a uniform ingress front in case of zero-minute time gaps and a more pronounced intrusion at the interfaces due to the higher porosity. In both cases, the intrusion is higher compared with the molded reference material. Both phenomena could be attributed to the higher porosity and the formation of microcracks at the surface of printed specimens as they are directly after printing prone to shrinkage and the increased surface area exposed to harmful substances;
- Based on potentiometric titrations, the non-steady state diffusion coefficient and the surface concentration were calculated by fitting the measurements by Fick's second law. Like conventional concrete, the diffusion coefficient shows a decrease over time, while the surface concentration shows an increase. A prolonged time gap increases the non-steady state diffusion coefficient;
- The main goal of the freeze/thaw investigations was to check whether or not the current Belgian standard NBN B 15 – 231 was applicable in case of 3D printed concrete. Based on the obtained results, no significant difference could be observed between printed or traditional manufactured elements. The freeze/resistance seems in addition independent of the applied time gap. The latter phenomenon could be explained based on the increased amount of air voids, present at the interface and in the bulk material, caused by the printing process. To make more conclusive statements, the number of freeze/thaw cycles have to be increased and more elaborated investigations of the size and distribution of the air voids are necessary.

CRedit authorship contribution statement

Jolien Van Der Putten: Conceptualization; Data curation; Formal analysis; Investigation; Methodology; Project administration; Resources; Software; Supervision; Validation; Visualization; Roles/Writing - original draft; Writing - review & editing.

Melissa De Volder: Data curation; Formal analysis; Investigation; Validation; Visualization.

Philip Van den Heede: Conceptualization; Methodology; Writing - review & editing.

Maxim Deprez: Data curation; Formal analysis; Writing - review & editing.

Veerle Cnudde: Writing - review & editing.

Geert De Schutter: Funding acquisition; Supervision; Writing - review & editing.

Kim Van Tittelboom: Conceptualization; Funding acquisition;

Methodology; Supervision; Validation; Writing - review & editing.

Declaration of competing interest

The authors declare no conflict of interest.

Acknowledgements

J. Van Der Putten would like to acknowledge the support by EFRO for the C3PO-project (B/15100/01). P. Van den Heede is a postdoctoral fellow of the Research Foundation-Flanders (FWO) and gratefully acknowledge for the financial support of projects No. 3E013917 and No. G062720N.

References

- [1] J. Kruger, A. du Plessis, G. van Zijl, An investigation into the porosity of extrusion-based 3D printed concrete, *Additive Manufacturing* 37 (2021), 101740.
- [2] J. Van Der Putten, et al., Microstructural characterization of 3D printed cementitious materials, *Materials* 12 (18) (2019).
- [3] N. Venkatesh, S. Hempel, V. Mechtcherine, Micro- and macroscopic investigations on the interface between layers of 3D printed cementitious elements, in: *International Conference on Advances in Construction Materials and Systems*, 2017, Chennai.
- [4] V.N. Nerella, S. Hempel, V. Mechtcherine, Effects of layer-interface properties on mechanical performance of concrete elements produced by extrusion-based 3D-printing, *Constr. Build. Mater.* 205 (2019) 586–601.
- [5] R.J.M. Wolfs, F.P. Bos, T.A.M. Salet, Hardened properties of 3D printed concrete: the influence of process parameters on interlayer adhesion, *Cem. Concr. Res.* 119 (2019) 132–140.
- [6] Y.W.D. Tay, et al., Time gap effect on bond strength of 3D-printed concrete, in: *Virtual and Physical Prototyping* 14, 2018, pp. 104–113.
- [7] S.C. Paul, et al., Fresh and hardened properties of 3D printable cementitious materials for building and construction, *Arch Civ Mech Eng* 18 (1) (2018) 311–319.
- [8] T.T. Le, et al., Hardened properties of high-performance printing concrete, *Cem. Concr. Res.* 42 (3) (2012) 558–566.
- [9] B. Van Belleghem, Effect of Capsule-based Self-healing on Chloride Induced Corrosion of Reinforced Concrete, PhD-thesis, 2018, Ghent.
- [10] P.C. Bran Anleu, Quantitative Micro XRF Mapping of Chlorides: Possibilities, Limitations, and Applications, from Cement to Digital Concrete, ETH, Zurich, 2018.
- [11] P. Van den Heede, Durability and Sustainability of Concrete With High Volumes of Fly Ash, Universiteit Gent, Gent, 2014.
- [12] M. Thiery, et al., Investigation of the carbonation front shape on cementitious materials: effects of the chemical kinetics, *Cem. Concr. Res.* 37 (7) (2007) 1047–1058.
- [13] M. Thiery, et al., Effect of carbonation on the microstructure and moisture properties of cement-based materials, in: *XII DBMC (12th International Conference on Building Materials and Components)*, 2011.
- [14] P.H. Borges, et al., Carbonation of CH and C-S-H in composite cement pastes containing high amounts of BFS, *Cem. Concr. Res.* 40 (2) (2010) 284–292.
- [15] M. Deprez, A Multiscale Experimental Identification of Freeze-thaw Induced Pore-scale Processes in Porous Mineral Building Materials, Universiteit Gent. Faculteit Wetenschappen, 2020.
- [16] C.-S. Shon, et al., Freezing and thawing resistance of cellular concrete containing binary and ternary cementitious mixtures, *Constr. Build. Mater.* 168 (2018) 73–81.
- [17] P.J. Tikalsky, J. Pospisil, W. MacDonald, A method for assessment of the freeze–thaw resistance of preformed foam cellular concrete, *Cem. Concr. Res.* 34 (5) (2004) 889–893.
- [18] W. Tian, N. Han, Pore characteristics (>0.1 mm) of non-air entrained concrete destroyed by freeze-thaw cycles based on CT scanning and 3D printing, *Cold Reg. Sci. Technol.* 151 (2018) 314–322.
- [19] B. Masschaele, et al., HECTOR: a 240kV micro-CT setup optimized for research, *J. Phys. Conf. Ser.* 463 (2013), 012012.
- [20] J. Vlassenbroeck, et al., Software tools for quantification of X-ray microtomography at the UGCT, *Nucl. Inst. Methods Phys. Res. A* 580 (1) (2007) 442–445.
- [21] 12390-11, C.T., Testing hardened concrete - part 11: testing hardened concrete - Part 11: determination of the chloride resistance of concrete: unidirectional diffusion, in: *European Committee for Standardization*, Brussels, 2007.
- [22] L. Real, et al., AgNO₃ spray method for measurement of chloride penetration: the state of art, *Revista ALCONPAT* 5 (2015) 142.
- [23] 12390-10, C.T., Testing hardened concrete - part 10: determination of the relative carbonation resistance of concrete, in: *European Committee for Standardization*, Brussels, 2007.
- [24] B15-231, N., Proeven op beton: vorstbestandheid, in: *Belgisch Instituut voor normalisatie*, Brussel, 1987.
- [25] N.E., Testing hardened concrete - part 3: compressive strength of test specimens, in: *Bureau voor Normalisatie*, Brussel, 2019.
- [26] G.M. Moelich, J. Kruger, R. Combrinck, Plastic shrinkage cracking in 3D printed concrete, *Compos. Part B* 200 (2020), 108313.

- [27] K. Audenaert, in: *Transportmechanismen in zelfverdichtend beton in relatie met carbonatie en chloridepenetratie*, Univeristy of Ghent, 2006, p. 369. PhD-dissertation.
- [28] M. Khanzadeh Moradllo, S. Sadati, M. Shekarchi, Quantifying maximum phenomenon in chloride ion profiles and its influence on service-life prediction of concrete structures exposed to seawater tidal zone – a field oriented study, *Constr. Build. Mater.* 108 (2018).
- [29] J. Liu, et al., Understanding the interacted mechanism between carbonation and chloride aerosol attack in ordinary Portland cement concrete, *Cem. Concr. Res.* 95 (2017) 217–225.
- [30] H. Friedmann, O. Amiri, A. Ait-Mokhtar, Physical modeling of the electrical double layer effects on multispecies ions transport in cement-based materials, *Cem. Concr. Res.* 38 (2008) 1394–1400.
- [31] Q. Qiu, A state-of-the-art review on the carbonation process in cementitious materials: fundamentals and characterization techniques, *Constr. Build. Mater.* 247 (2020), 118503.